

# Bio-inspired Approach for Long-Range Underwater Navigation Using Model Predictive Control

Yongding Zhang, Xiaofeng Liu, *Member, IEEE*, Minzhou Luo, and Chenguang Yang, *Senior Member, IEEE*

**Abstract**—Lots of evidence has indicated that many kinds of animals can achieve goal-oriented navigation by spatial cognition and dead reckoning. Geomagnetic field (GF) is a ubiquitous cue for navigation by these animals. Inspired by the goal-oriented navigation of animals, a novel long-distance underwater geomagnetic navigation (LDUGN) method is presented in this paper, which only utilizes the declination component ( $D$ ) and inclination component ( $I$ ) of GF for underwater navigation without any priori knowledge of geographical location or geomagnetic map. The  $D$  and  $I$  measured by high-precision geomagnetic sensors are compared periodically with that at the destination to determine the velocity and direction in the next step. A model predictive control (MPC) algorithm with control and state constraints is proposed to achieve the control and optimization of navigation trajectory. Because the optimal control is recalculated at each sampling instant, the MPC algorithm can overcome interferences of geomagnetic daily fluctuation, geomagnetic storms, ocean current, and geomagnetic local anomaly. The simulation results validate the feasibility and accuracy of the proposed algorithm.

**Index Terms**—Geomagnetic navigation, underwater navigation, bio-inspired, autonomous underwater vehicle (AUV), model predictive control (MPC).

## I. INTRODUCTION

UNDERWATER navigation technologies have been paid more and more attention because of broad applications in scientific exploration, commercial, military, rescue, surveying and mapping in the past decades [1]. Because the most common positioning and navigation technology, global positioning system (GPS), is not available in underwater environment,

the positioning and navigation of AUVs face greater challenge [2]. Many alternative technologies have been utilized for underwater navigation, such as inertial navigation system (INS), terrain-aided navigation, gravity-aided navigation, acoustic navigation and geomagnetic navigation [3], [4]. The INS uses sensors, such as accelerometers and gyroscopes, to continuously calculate the position, orientation, and velocity of a moving object by dead reckoning without external references [5]. However, the position error of INS gradually increases with time, which is fatal for a long-duration underwater navigation [6]. Many methods have been proposed to improve the accuracy of INS [7]–[10]. An embedded dynamics aiding technique was proposed to enhance the position, velocity, and attitude error estimations in INS [11]. By using information from a scanning sonar, the terrain-aided navigation compares the terrain features below the AUV with the known high resolution terrain map to estimate the location [12]. However, it is a difficult task to make the terrain map in advance [13], [14]. As a passive navigation technology, the gravity-aided navigation also requires a fairly accurate gravity map and is only suitable for regions with large variation of gravity characteristics [15], [16]. The acoustic navigation uses acoustic transponder beacons to determine position and has the advantages of high precision and no accumulated error, but it needs to deploy external transducers in advance, which is not suitable for applications such as ocean voyages [17], [18]. The geomagnetic navigation is a passive navigation technology with good concealment, low cost and no cumulative error. Geomagnetic matching is a conventional navigation technique, which can realize high precision positioning by comparing the geomagnetic profile acquired on board with the pre-stored geomagnetic map [19]. However, it strongly depends on a priori geomagnetic map, which is rather difficult to realize in practice for long distance underwater navigation [20].

It has been widely known that many animals have the ability to migrate or home across thousands of kilometers [21]. Homing pigeons released at a unacquainted place can fly hundreds of kilometers to return home [22]. The Pacific salmon can use geomagnetic cues to navigate to the correct coastal area from the open ocean in the final phase of their spawning migration [23]. It has been hypothesized that marine animals can imprint on the magnetic fields associated with their coastal reproductive areas and to use that information to return months or years later. Putman *et al.* [24] examined the geomagnetic imprinting hypotheses of natal homing with datasets that recorded variation in the migratory routes of salmon. It is speculated that salmon might assess location using a map sense based in part on magnetic intensity and inclination angle.

This work was supported in part by the National Natural Science Foundation of China under Grants 61473120 and 61803381, in part by the Key Research and Development Program of Jiangsu under Grants BE2017071, BE2017647, and BE2018004-04, in part by the Fundamental Research Funds for the Central Universities under Grant 2018B47114, in part by the Open Research Fund of State Key Laboratory of Bioelectronics of Southeast University under Grant 201905, in part by the State Key Laboratory of Integrated Management of Pest Insects and Rodents under Grant IPM1914, in part by the Projects of Anhui Province University Outstanding Youth Talent Support Program under Grant gxyq2019094, and in part by the Projects of International Cooperation and Exchanges of Changzhou under Grant CZ20170018. (*Corresponding author: Xiaofeng Liu.*)

Y. Zhang is with the College of Computer and Information, Hohai University, Nanjing 210098, China and with the School of Computer and Information Engineering, Chuzhou University, Chuzhou 239000, China (e-mail: ydzhang@chzu.edu.cn).

X. Liu is with the College of IoT Engineering, Hohai University, Changzhou 213022, China, with the Changzhou Key Laboratory of Robotis and Intelligent Technology, Changzhou 213022, China, and also with the Jiangsu Key Laboratory of Special Robots (Hohai University), Changzhou 213022, China (e-mail: xfliu@hhu.edu.cn).

M. Luo is with the Jiangsu Key Laboratory of Special Robots (Hohai University), Changzhou 213022, China (e-mail: lmz@hhuc.edu.cn).

C. Yang is with the Bristol Robotics Laboratory, University of the West of England, Bristol, BS16 1QY, UK. (e-mail: cyang@ieee.org).

Adult green turtles can detect geomagnetic information, which helps them return to their egg laying site [25]. In [26], the findings imply that sea turtles have a navigational system that exploits the geomagnetic field (GF) as a kind of bicoordinate magnetic map from which both longitudinal and latitudinal information can be extracted. In [27], the findings provide genetic corroboration of geomagnetic imprinting, and provide strong evidence that geomagnetic imprinting and magnetic navigation help shape the population structure of sea turtles and perhaps numerous other long-distance migrants that return to their natal areas to reproduce.

Inspired by the goal-oriented navigation of animals, different bio-inspired navigation strategies are proposed in the literatures. Fiack *et al.* [28] proposed an embedded architecture for bio-inspired vision-based robot navigation, which relies on visual attention to learn specific actions in each place. A fast and efficient homing algorithm based on Fourier transformed panoramic images was presented [29]. By continuously comparing Fourier coefficients calculated from the current view with coefficients representing the goal location, a mobile robot is able to find its way back to known locations. However, the vision-based methods have a huge workload of image processing, poor real-time performance and cannot work in dark environment. Taking inspiration from echolocating mammals, especially bats, a novel navigation technique was presented employing both multistatic and monostatic acoustic sensors [30]. However, the bio-inspired acoustic navigation need to place the transmitters beforehand, which is infeasible for long-distance navigation. A bio-inspired polarization navigation sensor was constructed to detect the polarization of skylight, and all the outputs are utilized to compute optimal angle estimation [31]. Inspired by the ant navigational strategies, a celestial compass was designed based on the linear polarization of ultraviolet skylight [32]. In [33], the geolocation of an observer can be determined based on radial underwater polarization patterns by using a bio-inspired polarization-sensitive imager. However, the structure of polarization navigation system is with high complexity and low accuracy. The geomagnetic matching navigation has high positioning accuracy and reliability, but it is obviously different from the way animals navigate. It seems that these marine animals do not need any large-scale spatial distribution of the GF, but only need the perceived real-time geomagnetic information during the navigation. Inspired by these phenomena, many biomimetic geomagnetic filtering navigation approaches are proposed. In [34], the navigation process is generalized as the convergence of geomagnetic multi-parameter from the present point values to the object point values, but the method was verified only under ideal conditions, without considering geomagnetic daily fluctuations and geomagnetic anomalies. To imitate animals' long-distance geomagnetic homing, an extended Kalman filter algorithm is introduced in [35] to estimate the location during navigation and is able to find a shortcut in the geomagnetic space. However, the method is not suitable for underwater navigation and the performance is very poor while passing through geomagnetic anomaly regions. The research works have confirmed the feasibility of underwater geomagnetic navigation, but navigation in geomagnetic anomalies region and

navigation trajectory optimization need to be further studied.

In this paper, the analysis of the GF is conducted and then a long-distance underwater geomagnetic navigation (LDUGN) method using model predictive control (MPC) is proposed. Without any assistance of prestored geomagnetic map or geographic information, we only use the realtime declination ( $D$ ) and inclination ( $I$ ) components of GF measured by geomagnetic sensors during the navigation. In the proposed MPC-based algorithm, the velocity and direction of the AUV are taken as manipulated variables, and the geomagnetic  $D$  and  $I$  are regarded as controlled variables. Simulations are conducted to validate our theoretical models and MPC-based algorithm. The results show that such a navigation method can find an optimal trajectory in GF space without being affected by interferences from geomagnetic daily fluctuation, geomagnetic storms, ocean current, and geomagnetic local anomalies.

The rest of this paper is organized as follows. The GF is introduced and analyzed in Section II. Section III presents details of our proposed LDUGN approach, followed by the simulations in Section IV. Finally, we conclude this paper in Section V.

## II. FUNDAMENTALS

### A. Description of the GF

The Earth is like a giant magnet. The GF is the Earth's natural resource and extends from the Earth's interior out into space [36], [37]. The intensity of GF ranges between approximately 25 and 65  $\mu\text{T}$  at the Earth's surface. It is widely accepted that the GF is produced by large-scale electric currents in the liquid outer core of the Earth consisting of highly conductive molten irons [38]. At every location on or above the Earth, the GF has a well-known direction, which can be used as a reference frame to orient ships, aircraft, satellites, antennas, drilling equipment and handheld devices [39].

As depicted in Fig. 1, the Earth is described by a spherical coordinate system. The GF vector is described by seven

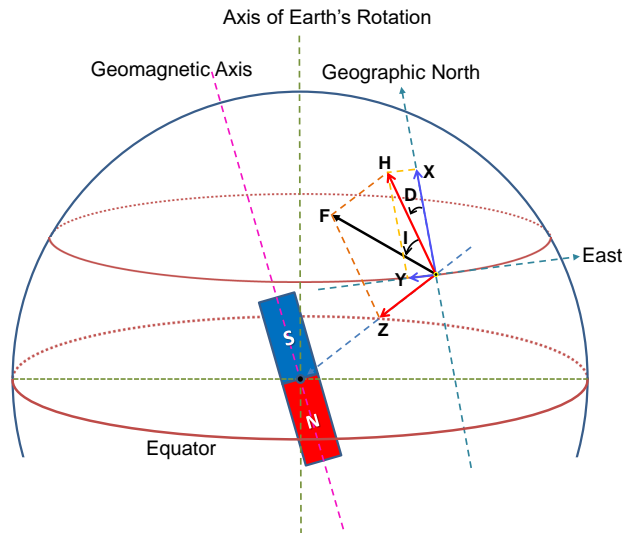


Fig. 1. Seven elements of the GF associated with an arbitrary point on the Earth.

elements. They are the northerly intensity  $X$ , the easterly intensity  $Y$ , the vertical intensity  $Z$ , the horizontal intensity  $H$ , the total intensity  $F$ , the inclination  $I$ , and the declination  $D$ , respectively. The GF currently tilts at an angle of about  $11^\circ$  with respect to the Earth's rotational axis, as if there were a bar magnet placed at that angle at the center of the Earth. As a result, the horizontal direction of the GF does not coincide with the direction of geographic north in most cases.

The GF is a function of space position and time. Many mathematical models have been designed to represent the Earth's magnetic field, such as the World Magnetic Model (WMM), the International Geomagnetic Reference Field Model (IGRF) and the Enhanced Magnetic Model (EMM). The WMM model is a spherical harmonic model and was developed jointly by the National Geophysical Data Center (NGDC, Boulder CO, USA) and the British Geological Survey (BGS, Edinburgh, Scotland). It has been widely used in civilian navigation systems [39]. In this paper, instead of measuring the real GF, we use the WMM2015 model to generate the realtime geomagnetic data, including  $D$  and  $I$ . The resolution of the GF intensity in WMM2015 model is 1 nT, and the distance resolution is  $0.01^\circ$  in latitude and longitude.

## B. Analysis of GF Data

1) *Geomagnetic Secular Variation*: The GF changes on time scales from milliseconds to millions of years. Shorter

time scales mostly arise from currents in the ionosphere and magnetosphere, and changes over time scales of a year or more mostly reflect the changes in the Earth's interior [40]. Secular variation can be observed in measurements at magnetic observatories, some of which have been in existence for hundreds of years. The direction and intensity of the dipole change over time. Over the last two centuries the dipole strength has been decreasing at a rate of about 6.3%. A prominent feature in the non-dipolar part of the secular variation is a westward drift at a rate of about  $0.2^\circ$  per year. Fig. 2 shows the annual variation of geomagnetic elements  $D$  and  $I$  at Beijing Ming Tombs Station and Sanya Station in 2014. It can be observed that the real geomagnetic variation is very slowly. In 2014, the geomagnetic  $D$  in Beijing Ming Tombs Station and Sanya Station increased by  $0.061^\circ$  and  $0.038^\circ$ , respectively (Fig. 2a). Correspondingly, the geomagnetic  $I$  in Beijing Ming Tombs Station and Sanya Station declined by  $0.079^\circ$  and  $0.159^\circ$ , respectively (Fig. 2b). This is highly suggestive of that it is feasible to use geomagnetic  $D$  and  $I$  measured by high-precision geomagnetic sensors for underwater navigation.

2) *Geomagnetic Declination and Inclination*: Geomagnetic  $D$  is the angle on the horizontal plane between the magnetic north and the geographic north. It varies with positions on the Earth's surface, and changes over time. By convention, the  $D$  is positive when magnetic north is to the east of geographic north, and negative when it is to the west. Geomagnetic  $I$  is the

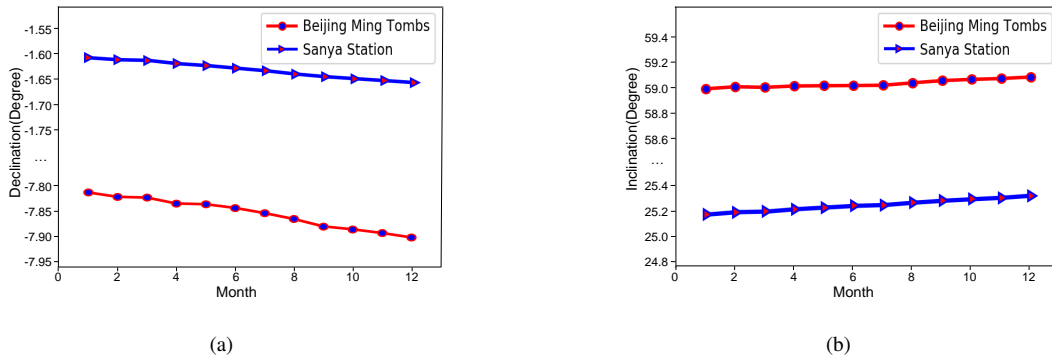


Fig. 2. Monthly Means of Declination and Inclination at Beijing Ming Tombs Station and Sanya Station in 2014. (a) Declination. (b) Inclination.

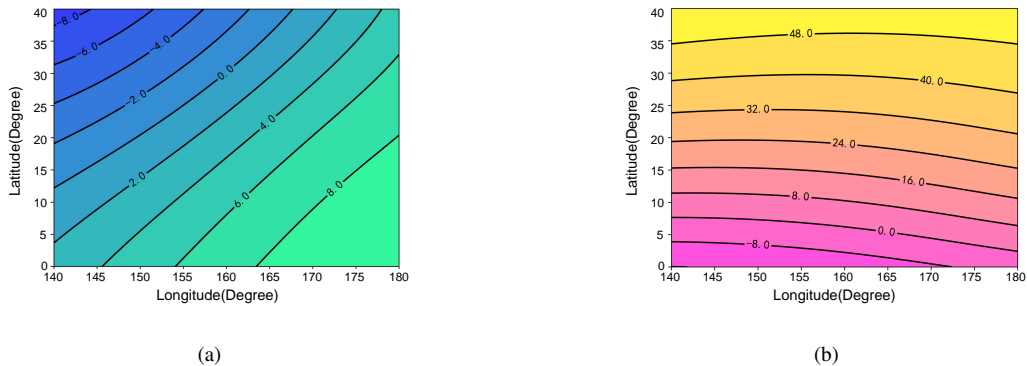


Fig. 3. Contour maps of Declination and Inclination of WMM2015 in the Pacific. (a) Declination. (b) Inclination.

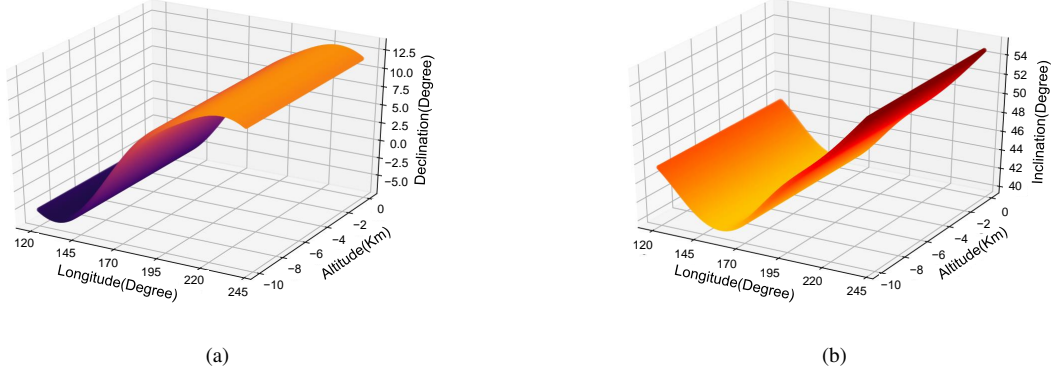


Fig. 4. Variations of Declination and Inclination in different altitudes underwater. (a) Declination. (b) Inclination.

angle made with the horizontal by the GF lines. It also varies at different points on the Earth's surface. The positive values of  $I$  indicate that the GF is pointing downward into the Earth at the points of measurement, and the negative values indicate that it is pointing upward [39]. Fig. 3 shows the contour map of  $D$  and  $I$  in the western Pacific region. In Fig. 3a, the  $D$  in this vast ocean area increases progressively to  $9.41^\circ$  from northwest to southeast from  $-8.81^\circ$ . Similarly, the  $I$  increases progressively to  $54.76^\circ$  from south to north from  $-16.12^\circ$  (Fig. 3b). This indicates that the  $D$  and  $I$  in the Pacific are unique, and a geographic position can be uniquely determined by a given geomagnetic  $D$  and  $I$ .

3) *Geomagnetic Spatial Variation*: The AUVs are at different heights below sea level during a mission. It is necessary to discuss the variation of GF in different depths below the surface of the water. The average depth of the Pacific Ocean is 3,957 meters with a maximum depth of 11,034 meters. This section mainly analyzes the space variation of underwater GF. Fig. 4 shows the variations of  $D$  and  $I$  in different altitudes underwater. For a given longitude and latitude, the variations of  $D$  (Fig. 4a) and  $I$  (Fig. 4b) is less than  $0.02^\circ$  in different altitudes underwater (from 0 km to -10 km), which can be ignored during long-range geomagnetic navigation.

### III. PROPOSED LDUGN APPROACH

In order to achieve long-distance underwater geomagnetic navigation, we assume that the  $D$  and  $I$  at the destination have been known before the navigation. The  $D$  and  $I$  at any location underwater can be obtained by geomagnetic sensors in real time. The hypotheses here are the same as [35]. In the course of geomagnetic navigation, the  $D$  and  $I$  measured in real time are compared with the  $D$  and  $I$  at the destination to determine whether the destination is reached or not. Unlike [35], we assume that the navigation occurs in the underwater environment, where it is not available to obtain the geographical direction by sun or constellations. During the navigation, a relative coordinate frame is established. The relative motion and direction can be obtained by means of highly sensitive triaxial accelerometers and gyroscopes, which have been studied and widely used in aviation, aerospace and navigation for several decades [41]–[43].

First of all, the process of LDUGN is described. The gradient of  $D$  and  $I$  at the origin is required at the beginning of navigation. As shown in Fig. 5, we move towards an arbitrary direction (denoted by  $x$ ) for a distance  $s_0$  and then move towards another direction (denoted by  $y$ ) which is  $90^\circ$  counterclockwise with  $x$  for another distance  $s_1$ . As a result, a rectangular coordinate frame ( $xoy$ ) is set up. The historic records of  $D$  and  $I$  at each location are saved and used to calculate the gradient of GF. According to the  $D$  and  $I$  at destination and the  $D$  and  $I$  at current location, the MPC-based method calculates the optimal velocity and motion direction at regular intervals. The geomagnetic navigation iterates until the differences of  $D$  and  $I$  between the current location and the destination are less than a preset value.

#### A. Problem Formulation

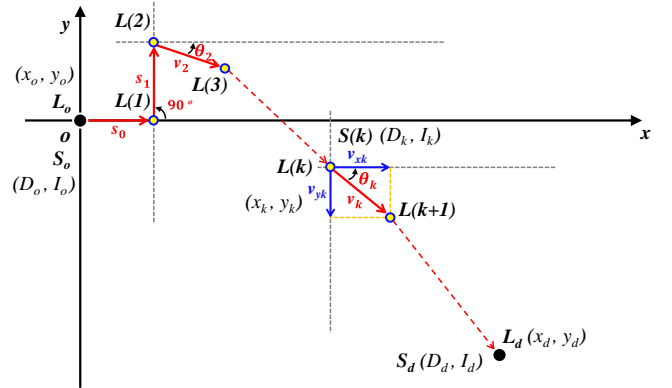


Fig. 5. Deduction of the bio-inspired geomagnetic navigation algorithm based on MPC.

As depicted in Fig. 5, we denote the  $k$ th sampling location by  $L(k) = [x_k, y_k]^T$ , where  $x_k$  and  $y_k$  represent the coordinates in the  $xoy$  coordinate frame.  $L_o = [x_o, y_o]^T$  and  $L_d = [x_d, y_d]^T$  represent the locations at the origin and the destination, respectively. The  $D$  and  $I$  at the  $k$ th sampling location are denoted by  $S(k) = [D_k, I_k]^T$ .  $S_o = [D_o, I_o]^T$

and  $S_d = [D_d, I_d]^T$  represent the  $D$  and  $I$  at the origin and the destination, respectively. During the navigation,  $S(k)$  can be obtained by shipborne high-precision geomagnetic sensors while arriving a new sampling location  $L(k)$ .  $v_k$  and  $\theta_k$  denote the velocity and the angle deviating from the  $x$  direction at the  $k$ th step, respectively.  $v_{xk}$  and  $v_{yk}$  are the components of  $v_k$  along the  $x$  direction and  $y$  direction, respectively.  $v_k$  and  $\theta_k$  can be calculated by

$$v_k = \sqrt{v_{xk}^2 + v_{yk}^2} \quad (1)$$

$$\theta_k = \pm \arctan \frac{v_{yk}}{v_{xk}}. \quad (2)$$

The gradient of  $D$  and  $I$  at the  $k$ th sampling location is denoted by  $G(k)$ , which can be expressed as

$$G(k) = \begin{bmatrix} d_{Dkx} & d_{Dky} \\ d_{I_kx} & d_{I_ky} \end{bmatrix} \quad (3)$$

where  $d_{Dkx}$ ,  $d_{Dky}$ ,  $d_{I_kx}$ ,  $d_{I_ky}$  denote the gradient of  $D$  along the  $x$  direction, the gradient of  $D$  along the  $y$  direction, the gradient of  $I$  along the  $x$  direction, the gradient of  $I$  along the  $y$  direction, respectively.

At the initial stage of the geomagnetic navigation, it is necessary to obtain the gradient of  $D$  and  $I$  around the origin. In [35], the gradient is obtained by the simple decomposition of the changes of  $D$  and  $I$  between two successive sampling locations in the east and north directions. However, the changes of  $D$  and  $I$  in the east and north directions are not well represented by the gradient since there is no certain relationship between the gradients in the east and north direction. On the contrary, there is a distinct difference in the contribution of  $D$  and  $I$  along two different directions in most cases. By analyzing the GF in the Pacific region, it can be found that the gradient of  $I$  in longitude direction is approximately 10 times that of latitude direction. As shown in Fig. 5, in order to obtain the gradient of  $D$  and  $I$  at  $L(2)$  (around the origin), we move from  $L_o$  along arbitrary direction (denoted by  $x$ ) to  $L(1)$  at first. Then we go on moving to  $L(2)$  along the direction (denoted by  $y$ ) which is  $90^\circ$  counterclockwise with the  $x$  direction. Therefore, the gradients of  $D$  and  $I$  at  $L(2)$  can be calculated as

$$d_{D2x} = \frac{D_1 - D_0}{x_1 - x_0} \quad (4)$$

$$d_{D2y} = \frac{D_2 - D_1}{y_2 - y_1} \quad (5)$$

$$d_{I2x} = \frac{I_1 - I_0}{x_1 - x_0} \quad (6)$$

$$d_{I2y} = \frac{I_2 - I_1}{y_2 - y_1}. \quad (7)$$

Because an extra moving distance is needed for calculating the gradient, it is a waste of time and cost to obtain the gradient at each sampling location. In this study, the gradient is calculated once only at the beginning of navigation, and then updated with the newly acquired  $D$  and  $I$  at each sampling location. In a real navigation, the gradient should be recalculated after a long voyage in order to improve the

navigation accuracy. The gradient at the  $(k+1)$ th sampling location can be approximately updated by

$$G(k+1) = G(k) + \begin{bmatrix} \Delta D_{k+1} \\ \Delta I_{k+1} \end{bmatrix} \begin{bmatrix} \cos^2 \theta_k & \sin^2 \theta_k \\ \frac{v_{xk} T}{v_{yk} T} & \frac{v_{yk} T}{v_{xk} T} \end{bmatrix} \quad (8)$$

with

$$\Delta D_{k+1} = D'_{k+1} - D_{k+1} \quad (9)$$

$$\Delta I_{k+1} = I'_{k+1} - I_{k+1} \quad (10)$$

where  $D'_{k+1}$  and  $I'_{k+1}$  are the  $D$  and  $I$  measured by geomagnetic sensors at the  $(k+1)$ th sampling location,  $D_{k+1}$  and  $I_{k+1}$  are the  $D$  and  $I$  estimated by the gradient  $G(k)$  at the  $(k+1)$ th sampling location,  $T$  is the sampling period.

### B. MPC Algorithm

MPC is an optimal control strategy based on numerical optimization, which utilizes an explicit process model to predict the future response of a plant. At each control interval the MPC method attempts to optimize future plant behavior by computing a sequence of future manipulated variable adjustments. The optimal control inputs of the next  $N$  sampling instants are obtained by minimizing a cost function. The outputs of the future  $N$  sampling instants are predicted according to the system model, and the cost function is constructed based on the errors between the predicted outputs and the true state outputs of the system [44]. The input and state constraints are considered to improve the robustness of the system. Particularly, the MPC algorithm can handle multivariate and constrained problems effectively [45]. In this section, a MPC-based geomagnetic navigation strategy is designed to ensure that the AUV can reach the destination along an optimal trajectory in geomagnetic space.

First, the future state of the controlled AUV is predicted using a dynamic model. Let  $S(k) = [D_k, I_k]^T$  and  $u(k) = [v_{xk}, v_{yk}]^T$  be the model state and input vectors, where  $D_k$ ,  $I_k$ ,  $v_{xk}$  and  $v_{yk}$  represent the geomagnetic declination, the geomagnetic inclination, the velocity component along the  $x$  direction and velocity component along the  $y$  direction at the  $k$ th sampling location, respectively. Based on zero-order hold (ZOH), a continuous-time system can be transformed into a discrete-time form with a sampling period  $T$

$$S(k+1) = S(k) + \dot{S}T \quad (11)$$

where

$$\dot{S} = G(k)u(k). \quad (12)$$

The discrete-time system model (11) can be expressed with MPC state-space representation

$$S(k+1) = AS(k) + B(k)u(k) \quad (13)$$

with

$$A = I_2 \quad (14)$$

$$B(k) = G(k)T \quad (15)$$

where  $I_2$  denotes a 2-by-2 constant identity matrix, and  $B(k)$  is a 2-by-2 matrix that determined by geomagnetic gradient

$G(k)$  dynamically. Based on the state-space model, the MPC algorithm is designed to control the system.

In the real navigation, the control input and system state have hard constraints. Fortunately, the MPC algorithm can provide a systematic method of dealing with constraints on input and state. These constraints are accounted for explicitly by solving a constrained optimization problem in real-time to determine the optimal predicted inputs. In this study, the control input  $u(k)$  and the state  $S(k)$  are constrained. Thus, the following constraints should be imposed on the system.

$$u_{min} \leq u(k) \leq u_{max}, \quad S_{min} \leq S(k) \leq S_{max} \quad (16)$$

where  $u_{min}$ ,  $u_{max}$ ,  $S_{min}$  and  $S_{max}$  are the preset lower bound of input, the preset upper bound of input, the preset lower bound of state, the preset upper bound of state, respectively.

Given a predicted input sequence, the corresponding sequence of state predictions can be calculated by simulating the model forward over the prediction horizon (denoted by  $N$ ). For notational convenience, these predicted sequences are stacked into vectors  $\bar{U}(k)$ ,  $\bar{S}(k)$  defined by

$$\bar{U}(k) = \begin{bmatrix} u(k|k) \\ u(k+1|k) \\ \vdots \\ u(k+N-1|k) \end{bmatrix}, \quad \bar{S}(k) = \begin{bmatrix} S(k+1|k) \\ S(k+2|k) \\ \vdots \\ S(k+N|k) \end{bmatrix} \quad (17)$$

where  $u(k+i|k)$  and  $S(k+i|k)$  denote the input and state vectors at time  $k+i$  which are predicted at time  $k$ .

By analyzing the geomagnetic data from WMM2015, it can be found that the geomagnetic gradient changes very slowly within hundreds of kilometers (see Fig. 6). For this reason, in order to reduce the computational effort, we assume that the geomagnetic gradient  $G(k)$  and coefficient  $B(k)$  are invariant in the future  $N$  sampling instants. According to (13), we can predict the future state  $S(k+i|k)$  ( $i = 1, 2, \dots, N$ ) at sampling instant  $k$  as follows:

$$\begin{aligned} S(k+1|k) &= AS(k|k) + B(k)u(k|k) \\ S(k+2|k) &= AS(k+1|k) + B(k)u(k+1|k) \\ &\vdots \\ S(k+N|k) &= AS(k+N-1|k) + B(k)u(k+N-1|k) \end{aligned} \quad (18)$$

with initial condition  $S(k|k) = S(k)$  and  $u(k|k) = u(k)$ .

Therefore, the relationship between  $\bar{S}(k)$  and  $\bar{U}(k)$  can be described as

$$\bar{S}(k) = HS(k) + P(k)\bar{U}(k) \quad (19)$$

where

$$H = [A, A^2, \dots, A^N]^T \quad (20)$$

$$P(k) = \begin{bmatrix} B(k) & 0 & \dots & 0 \\ AB(k) & B(k) & \dots & 0 \\ \vdots & \vdots & \ddots & \vdots \\ A^{N-1}B(k) & A^{N-2}B(k) & \dots & B(k) \end{bmatrix}. \quad (21)$$

By taking into account (15),  $P(k)$  can be rewritten as

$$P(k) = \begin{bmatrix} G(k)T & 0 & \dots & 0 \\ AG(k)T & G(k)T & \dots & 0 \\ \vdots & \vdots & \ddots & \vdots \\ A^{N-1}G(k)T & A^{N-2}G(k)T & \dots & G(k)T \end{bmatrix} \quad (22)$$

The predictive control feedback law is computed by minimizing a predicted performance cost function, which can be optimized to obtain the optimal control sequence in the predictive horizon  $N$ . The predicted cost function has the form

$$\begin{aligned} J(k) &= \sum_{i=1}^N [\|S(k+i|k) - S_d\|_Q^2 + \|u(k+i-1|k)\|_R^2] \quad (23) \\ &= \sum_{i=1}^N [(S(k+i|k) - S_d)^T Q (S(k+i|k) - S_d) \\ &\quad + u^T(k+i-1|k) R u(k+i-1|k)] \quad (24) \end{aligned}$$

where  $\|\cdot\|$  denotes the Euclidean norm;  $Q$  and  $R$  are the symmetric definite-positive weight matrices;  $S(k+i|k)$  and  $u(k+i-1|k)$  are the estimated state and input vectors at time  $k+i$  which are predicted at time  $k$ ,  $S_d$  is the desired state vector at the destination.

Substituting (19) into (24) yields

$$J(k) = \|\bar{S}(k) - \bar{S}_d\|_{\bar{Q}}^2 + \|\bar{U}(k)\|_{\bar{R}}^2 \quad (25)$$

$$= \|HS(k) + P(k)\bar{U}(k) - \bar{S}_d\|_{\bar{Q}}^2 + \|\bar{U}(k)\|_{\bar{R}}^2 \quad (26)$$

with

$$\begin{aligned} \bar{S}_d &= [S_d, S_d, \dots, S_d]^T \\ \bar{Q} &= \text{diag}(Q, Q, \dots, Q) \\ \bar{R} &= \text{diag}(R, R, \dots, R) \end{aligned}$$

where  $\text{diag}(\cdot)$  denotes the diagonal matrix.

From (26), it can be easily seen that  $J(k)$  is a function of  $\bar{U}(k)$ . Then, the optimization problem is formulated as follows:

$$\min_{\bar{U}(k)} \|HS(k) + P(k)\bar{U}(k) - \bar{S}_d\|_{\bar{Q}}^2 + \|\bar{U}(k)\|_{\bar{R}}^2 \quad (27)$$

$$\text{s.t.} \quad \bar{U}_{min} \leq \bar{U}(k) \leq \bar{U}_{max} \quad (28)$$

$$\bar{S}_{min} \leq HS(k) + P(k)\bar{U}(k) \leq \bar{S}_{max} \quad (29)$$

where

$$\begin{aligned} \bar{U}_{min} &= [u_{min}, u_{min}, \dots, u_{min}]^T \\ \bar{U}_{max} &= [u_{max}, u_{max}, \dots, u_{max}]^T \\ \bar{S}_{min} &= [S_{min}, S_{min}, \dots, S_{min}]^T \\ \bar{S}_{max} &= [S_{max}, S_{max}, \dots, S_{max}]^T. \end{aligned}$$

Then, constraints (28) and (29) can be rewritten in a compact form as follows:

$$C\bar{U}(k) \leq c \quad (30)$$

where

$$C = \begin{bmatrix} I_{2N} \\ -I_{2N} \\ P(k) \\ -P(k) \end{bmatrix}, \quad c = \begin{bmatrix} \bar{U}_{max} \\ -\bar{U}_{min} \\ \bar{S}_{max} - HS(k) \\ -\bar{S}_{min} + HS(k) \end{bmatrix}. \quad (31)$$

It is a rather complicated issue to obtain the solution of the optimization problem (27). Fortunately, we can further convert it into a convex quadratic programming (QP) problem via a series of simple transformations. The convex QP optimization problem has been studied for several decades, and can be solved by the contemporary methods such as interior point method, augmented Lagrangian method and conjugate gradient method [46]. Therefore, (27) is transformed into a standard convex QP form as follow:

$$\min_{\bar{U}(k)} \frac{1}{2} \bar{U}^T(k)W(k)\bar{U}(k) + M^T(k)\bar{U}(k) \quad (32)$$

$$s.t. \quad C\bar{U}(k) \leq c \quad (33)$$

where

$$W(k) = 2(P^T(k)\bar{Q}P(k) + \bar{R}) \quad (34)$$

$$M(k) = P^T(k)\bar{Q}(HS(k) - \bar{S}_d). \quad (35)$$

It has been proved that the standard convex QP optimization problem has a unique optimal solution [47]. The solution of (32), denoted by  $u^*(k)$ , can be readily computed online by a QP solver in matlab. Then, an optimal control sequence is obtained. In order to enhance the robustness of the LDUGN approach, only the first control in the optimal control sequence is executed by the AUV, and the entire calculation is repeated at every subsequent control intervals. The MPC optimization process iterates until the difference of the states at the current location and the destination is less than a preset value (denoted by  $\varepsilon$ ).

The complete navigation algorithm is summarized in Algorithm 1.

---

#### Algorithm 1 MPC-based Underwater Navigation Algorithm

**Input:**  $S_o$  (original state),  $S_d$  (final state),  $N$  (prediction horizon),  $A$  (coefficient matrix),  $Q, R$  (weighting matrices),  $u_{min}, u_{max}$  (control constraints),  $S_{min}, S_{max}$  (state constraints)

- 1:  $k \leftarrow 1$
  - 2:  $S(k) \leftarrow S_o$
  - 3: Calculate  $G(k)$  by Eqs. (3)-(7)
  - 4: **while**  $|S(k) - S_d| \geq \varepsilon$  **do**
  - 5:   Solve the optimization problem in (32) and (33)
  - 6:   Get the first control input from  $u^*(k)$
  - 7:   Calculate  $v_k$  and  $\theta_k$  by Eqs. (1) and (2)
  - 8:   Apply control input  $v_k$  and  $\theta_k$
  - 9:   Update  $G(k)$  by Eq. (8)
  - 10:  $k \leftarrow k + 1$
  - 11:   Get  $S(k)$
  - 12: **end while**
- 

## IV. SIMULATIONS

In this section, simulations are carried out to verify the performance of the proposed LDUGN algorithm. All simulations are performed on a personal laptop (CPU: Intel(R) Core(TM) i5-4220U: 2.30GHz; RAM: 4.00GB) using a simulator developed on Matlab R2017a platform. The simulation results show that the maximum, minimum, and average computation time

for the optimization problem are 0.078s, 0.012s, and 0.026s, respectively. Compared with the sampling period  $T = 1$  hour, the computation time is acceptable for real-time navigation. In these simulations, we choose a rectangular area in the vast western Pacific (see the inset in Fig. 7), which is from  $0^\circ$  north latitude,  $140^\circ$  east longitude ( $0^\circ\text{N}, 140^\circ\text{E}$ ) to  $40^\circ$  north latitude,  $180^\circ$  east longitude ( $40^\circ\text{N}, 180^\circ\text{E}$ ). According to the geomagnetic contour maps (see Fig. 3), the geographical coordinates of the area can be uniquely determined by the  $D$  and  $I$  values. In the single-destination scenario, we choose ( $30^\circ\text{N}, 145^\circ\text{E}$ ) as the origin and ( $5^\circ\text{N}, 175^\circ\text{E}$ ) as the destination, the states of which are  $[-4.54, 41.03]^T$  and  $[9.05, 3.19]^T$ , respectively. In all scenarios, the real-time geomagnetic  $D$  and  $I$  data are retrieved from the WMM2015 model.

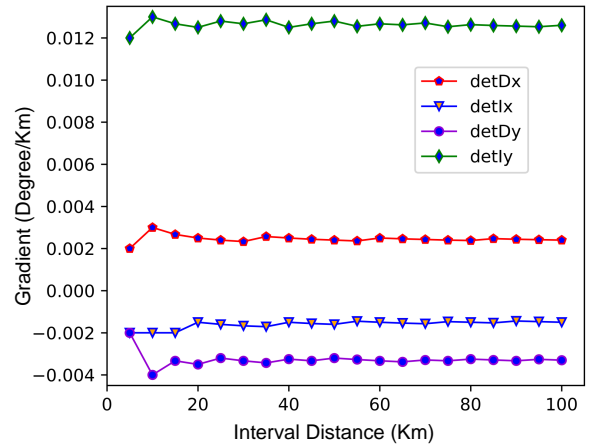


Fig. 6. Gradient variations of Declination and Inclination with different interval distance in x and y direction.

At the beginning of the navigation, the AUV need to move along two arbitrary mutually perpendicular directions to obtain the gradient of  $D$  and  $I$  at the origin. Due to the slow changes of  $D$  and  $I$ , the actual gradient cannot be obtained if the distance is too short. Although long distance can get more accurate gradient, it is a waste of time and cost. In order to get a more appropriate moving distance, a simple experiment has been carried out. The experiment shows the change of gradient of  $D$  and  $I$  in the  $x$  and  $y$  directions when the moving distance changes from 5 km to 100 km. As can be seen from Fig. 6, when the interval distance is less than 20 km, the gradient changes greatly, which means the gradient is local and cannot represented the gradient of this area. The gradient tends to be stable when the interval distance is greater than 20 km. As a result, we choose 10 nautical miles (nmi, about 18.52 km) as the interval distance in subsequent simulations.

In recent years, various AUVs have been designed and developed. The speed of latest AUV can reach more than 40 knots. In our simulations, we set the max speed of AUV along two directions to 40 knots at the beginning of navigation. In order to get a better navigation accuracy, the max speed is changed to 20 knots when the differences of  $D$  and  $I$  between the current location and the destination are less than  $1^\circ$ . The max speed is changed to 10 knots when the differences are

less than  $0.1^\circ$ . If the differences of  $D$  and  $I$  are less than  $0.01^\circ$ , we consider that the AUV has arrived the destination, and then the navigation is finished.

The rest of the parameters for simulations are set as follows: the sampling period  $T=1$ ; the prediction horizon  $N=20$ ; the weighting matrices  $Q=\text{diag}(10, 10)$  and  $R=\text{diag}(10^{-3}, 10^{-3})$ ; the original state  $S_o=[-4.54, 41.03]^T$  and the target state  $S_d=[9.05, 3.19]^T$ ; the lower bound of state  $S_{min}=[-8, -10]^T$  and the upper bound of state  $S_{min}=[10, 54]^T$ .

### A. Simulation without Interferences

In the ideal situation, any interferences are not considered during the geomagnetic navigation. As shown in Fig. 7, the navigation is started from  $(30^\circ\text{N}, 145^\circ\text{E})$ , where the state is  $[-4.54, 41.03]^T$ . The  $D$  and  $I$  at the destination are  $9.05^\circ$  and  $3.19^\circ$ , respectively. First, we move 10 nmi along a direction (denoted by  $x$ ), and then move 10 nmi along another direction (denoted by  $y$ , rotate  $90^\circ$  counterclockwise from the  $x$  direction). The coordinates of the two locations are about  $(30^\circ\text{N}, 145.17^\circ\text{E})$  and  $(30.17^\circ\text{N}, 145.17^\circ\text{E})$ , respectively. The states are  $[-4.49, 41]^T$  and  $[-4.56, 41.29]^T$ , respectively. According to the states of the first three locations, the geomagnetic gradient around the origin is calculated by (3)-(7). The gradient  $G(2)=[0.0025, -0.0035; -0.0015, 0.0145]$ . Then, the current geomagnetic state  $S(2)$ , the geomagnetic state at the destination  $S_d$  and the current geomagnetic gradient  $G(2)$  are input into the MPC algorithm to get the optimal control sequence. At location  $(30.17^\circ\text{N}, 145.17^\circ\text{E})$ , the optimal control sequence is obtained through solving the QP problem (32). We choose the first element  $[10.8, -40]^T$  in the optimal control sequence as our input. After reaching the next location  $(29.51^\circ\text{N}, 145.35^\circ\text{E})$ , we get the local state  $[-4.29, 40.26]^T$ , update the magnetic gradient  $G$  by (8), and then get the optimal control sequence. In Fig. 8, the trajectories of the control inputs are illustrated. As can be seen from this figure, the control inputs never transcend the boundary. The absolute values of the velocity component  $v_x$  and  $v_y$  decrease gradually while approaching the destination.

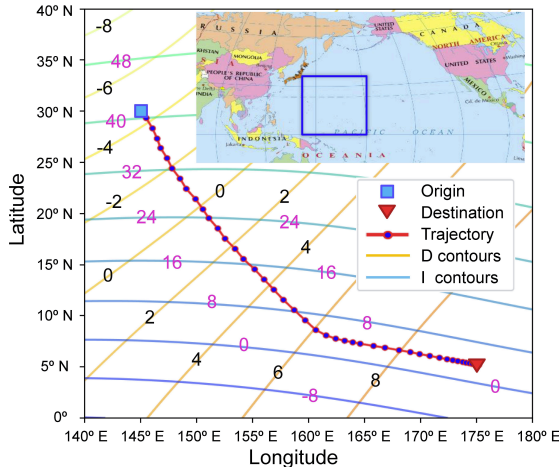


Fig. 7. Simulation of geomagnetic navigation without interferences.

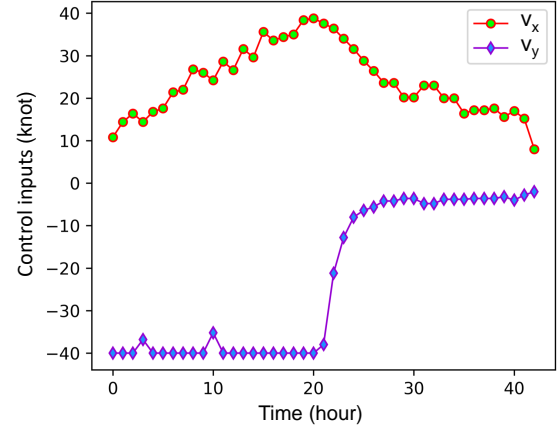


Fig. 8. Trajectories of control inputs without interferences.

The process is iterated until the location is near enough from the destination. Finally, the navigation ends at the location  $(5.01^\circ\text{N}, 174.91^\circ\text{E})$ , which is 5.43 nmi away from the destination. The error is extremely small relative to the total navigation distance (about 2340 nmi). The simulation result shows that our approach work well and can find a shortcut in geomagnetic space.

### B. Simulation with the Daily Fluctuation of GF

The GF shows distinct periodicity ranging from a few seconds to several thousand years. Variations with periodicities less than three years cannot possibly be of internal origin as these are effectively screened by the Earth's mantle [48]. The daily variations of the GF are mainly caused by the change of the ionosphere and magnetic layer current system in the outer space of the Earth. The quiet day daily variation range of the GF increases with solar activity. However, the daily ranges of the GF at different latitudes in the same longitude zone do not correlate very well. Generally, the variation rule of the GF is that the diurnal variation is large and the nocturnal variation is small. Meanwhile, the daily variation is large in summer and small in winter. In this section, a simulation is carried out under the quiet day geomagnetic daily variation. Because of the daily fluctuation, the  $D$  and  $I$  measured by geomagnetic sensors, as well as the gradient, will bring errors into our model.

In this simulation, a geomagnetic navigation is performed under interferences which are added on  $D$  and  $I$  as a Gaussian white noise with a standard deviation of  $1^\circ$  to imitate the aforementioned fluctuation with the maximum range [35]. The purple line in Fig. 9 shows the traveling trajectory under the interferences. For comparison, the traveling trajectory under interferences which are added on  $D$  and  $I$  as a Gaussian white noise with a standard deviation of  $0.5^\circ$  is also plotted in green line. The results indicate that all the simulations can be carried out successfully, arriving at locations  $(5.14^\circ\text{N}, 174.64^\circ\text{E})$  (with  $1^\circ$  interferences) and  $(4.92^\circ\text{N}, 174.88^\circ\text{E})$  (with  $0.5^\circ$  interferences), which is 23.17 nmi and 8.65 nmi

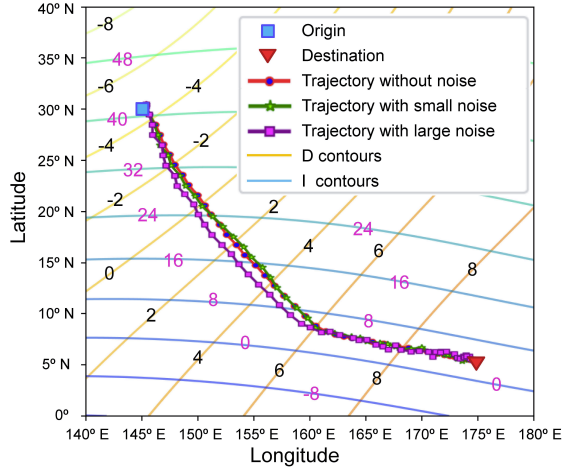


Fig. 9. Simulation of geomagnetic navigation under the GF's daily fluctuation.

far away from the destination, respectively. The errors are still small compared with the total navigation distance (about 2340 nmi).

### C. Simulation with the Geomagnetic Storms

A geomagnetic storm is a temporary global disturbance of the Earth's magnetosphere caused by a solar wind shock wave or cloud of magnetic field that interacts with the GF [49]. The global disturbance may last for more than ten hours to tens of hours. During the geomagnetic storm, all geomagnetic components change drastically, and the geomagnetic horizontal component  $H$  changes mostly. A geomagnetic storm has three phases: initial, main and recovery. At the initial phase, the  $H$  value at low and middle latitudes shows a rise in a few minutes. The rise may persist for anything from a few minutes to several hours before it drops back to the pre-impact level. The main phase is the most spectacular part of a geomagnetic storm. In low latitudes, the  $H$  value drops back to the initial level and then dip down far below it in a few hours. The recovery phase is when the  $H$  value changes from its minimum to its quiet time value. The recovery phase may last as short as 8 hours or as long as 7 days.

In order to verify the validity of the algorithm during a geomagnetic storm, the simulations are carried out in two scenarios. Because the initial phase was of short duration, it can be neglected in the long-distance navigation. In the first scenario, the geomagnetic storm occurs throughout the whole navigation. In the second scenario, the geomagnetic storm starts at the 10th hour and fades away at the 30th hour of the geomagnetic navigation. In [35], a geomagnetic storm is considered as  $1^\circ$  constant increase in  $D$ . In this section, the all time disturbance of geomagnetic storm (denoted by  $da(k)$ ) is defined as follow:

$$da(k) = \begin{cases} [1, 1]^T, & 0 < k \leq 10 \\ [(100-k)/90, (100-k)/90]^T, & 10 < k \leq 100 \\ [0, 0]^T, & k > 100 \end{cases}$$

and the part time disturbance of geomagnetic storm (denoted by  $dp(k)$ ) is defined as follow:

$$dp(k) = \begin{cases} [0, 0]^T, & 0 < k \leq 9 \\ [1, 1]^T, & 9 < k \leq 13 \\ [(30-k)/16, (30-k)/16]^T, & 13 < k \leq 30 \\ [0, 0]^T, & k > 30 \end{cases}$$

where  $k$  denote the sampling instant.

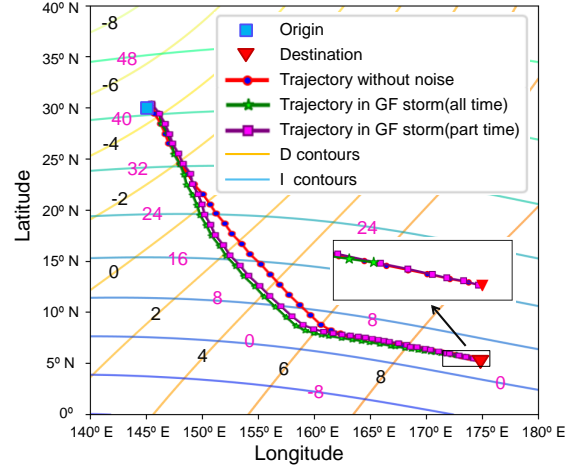


Fig. 10. Simulation of geomagnetic navigation during the geomagnetic storm.

The simulation result are shown in Fig. 10. The green line represents the navigation trajectory with the geomagnetic storm existing all time. The geomagnetic navigation stops at (5.40°N, 173.11°E), which is 116 nmi far from the destination. The result shows that our algorithm is greatly affected during the geomagnetic storms. This is because whether the navigation stop is determined by the geomagnetic  $D$  and  $I$ , but the  $D$  and  $I$  measured by geomagnetic sensors is strongly influenced by the geomagnetic storm. The navigation path in the second scenario are denoted by purple line, and the geomagnetic navigation finally stops at (5.01°N, 174.92°E), which is 4.84 nmi far from the destination. This means that our method is valid if the magnetic storm stops before the navigation ends. We find that the result is the same as simulation without interferences. This is because our MPC-based method is recalculated at each sampling location.

### D. Simulation with Position Drift

The water under the ocean is not static. Ocean current is a natural phenomenon in which sea water flows on a large scale along certain routes. It is generated by forces acting upon the water, such as the wind, the coriolis effect and the unevenness of the density distribution of sea water caused by the hot salt effect. Considering the North Pacific Gyre, simulations are done with different errors in velocity and direction throughout the whole navigation.

The purple line in Fig. 11 indicates the navigation path with 10 nmi/h constant errors in velocity to the northeast. For comparison, the traveling trajectory with inconstant errors in velocity is also plotted in green line. The drift direction is

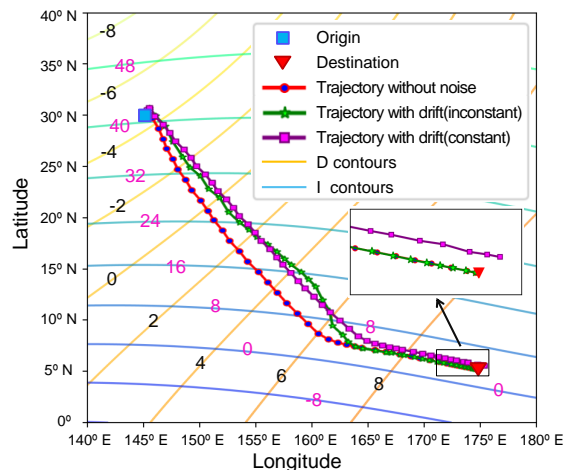


Fig. 11. Simulation of geomagnetic navigation with position drift.

east when the latitude is greater than  $20^\circ$ , the drift direction is northeast when the latitude is between  $10^\circ$  and  $20^\circ$ , and the drift fades away when the latitude is less than  $10^\circ$ . It can be seen that, with different errors, all the geomagnetic navigation can be successfully performed. The AUV arrived at the locations  $(5.38^\circ\text{N}, 175.49^\circ\text{E})$  with constant errors and  $(5.01^\circ\text{N}, 174.92^\circ\text{E})$  with inconstant errors, about 37.20 nmi and 4.84 nmi away from the destination, respectively. The error of 33.48 nmi is relatively large. This is because the speed of the AUV is rather slow at the end of navigation, and it can be avoided by increasing the speed of the AUV. As can be seen from Fig. 11, the simulation result with position drift is better than that without error. This is mainly because the position drift errors makes the AUV to shift northeast by coincidence. While arriving at the new location, our MPC-based algorithm will recalculate the optimal control according to the states at current location and the destination, so the position drift does not influence the geomagnetic navigation.

#### E. Simulation with Local-Area GF Anomaly

The geomagnetic anomaly refers to the additional magnetic field produced by magnetization of rocks with different magnetic properties in the Earth's crust. The magnetic anomalies are ubiquitous in nature. In this simulation, we assume that the geomagnetic navigation will pass by a region with geomagnetic anomaly. We added a  $1^\circ$  constant interference in geomagnetic  $D$  and  $I$  in the rectangular anomalous area from  $(10^\circ\text{N}, 150^\circ\text{E})$  to  $(20^\circ\text{N}, 160^\circ\text{E})$  (see the gray rectangular in Fig. 12).

As shown in Fig. 12, the AUV is still on the correct navigation path while passing the geomagnetic anomaly region. Finally, the navigation ends at the location 4.35 nmi far away from the destination. This is because our navigation algorithm is independent of the historical geomagnetic  $D$  and  $I$ . The MPC-based algorithm is used to get the optimal direction and velocity of the AUV periodically based on the current value of  $D$  and  $I$ . The performance of our method in the GF anomaly is better than the EKF-based method, in which

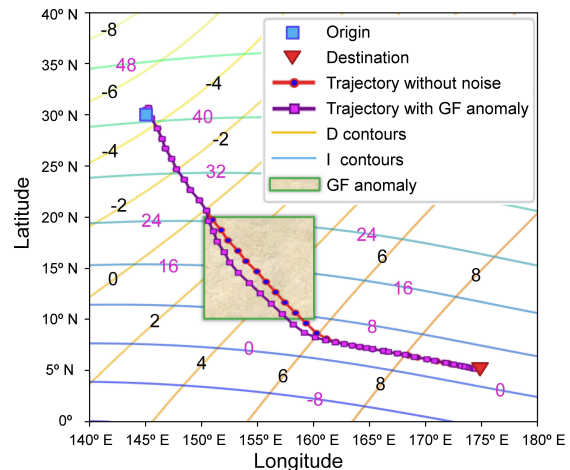


Fig. 12. Simulation of geomagnetic navigation through geomagnetic anomaly area.

the traveling path bypass the anomaly area along a zigzag route slowly. The EKF-based method does not enter the region while encountering geomagnetic anomaly, but moves along the boundary of the region, which obviously reduces the navigation efficiency.

#### F. Simulation with Multi-Destination Navigation

In some practical applications, the AUV is required to cruise under the ocean regularly. In this scenario, there may be several destinations to visit during a cruise mission. In this section, the feasibility and effectiveness of the multi-destination underwater navigation are verified. The state and location at the origin are  $[-2.83, 33.36]^T$  and  $(25^\circ\text{N}, 145^\circ\text{E})$ , respectively. The states at the destinations are  $[5.62, 7.5]^T$ ,  $[6.07, 28.01]^T$  and  $[0.06, 40.44]^T$ , respectively. The geographical locations of the destinations are  $(10^\circ\text{N}, 160^\circ\text{E})$ ,  $(20^\circ\text{N}, 170^\circ\text{E})$  and  $(30^\circ\text{N}, 160^\circ\text{E})$ , respectively. The AUV is needed to return back to the origin when the navigation ends.

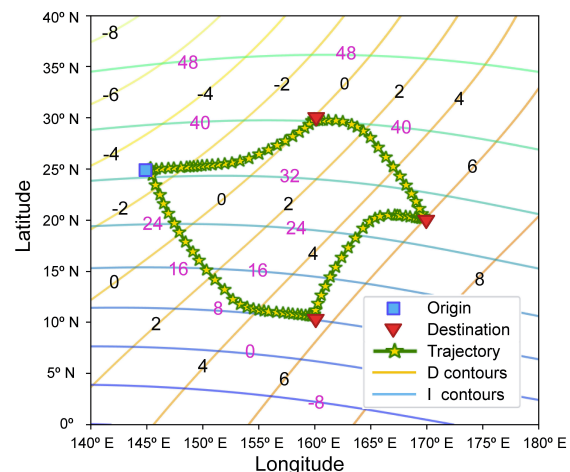


Fig. 13. Simulation of geomagnetic navigation of Multi-destination cruise.

In Fig. 13, each destination is visited under a shortcut path in geomagnetic space during the navigation. The errors are 5.43 nmi, 5.43 nmi, 7.02 nmi and 6.04 nmi, respectively. For thousands of nautical miles of voyage, the errors are rather small and acceptable. When arriving at several nautical miles near the destination, we can integrate our method with other navigation methods, such as terrain-based method and gravity-assisted navigation techniques, to improve the accuracy of our navigation.

## V. CONCLUSION

In this paper, a MPC-based geomagnetic navigation method is proposed for long-distance underwater voyage. In the LDUGN approach, none of priori knowledge of the geomagnetic map nor the geographic location is required. The feasibility of LDUGN is verified in the vast region of west Pacific based on the data retrieved from the WMM2015 model in real time. The navigation processes and simulation results have been presented and discussed in detail. The MPC algorithm is introduced in LDUGN to calculate the optimal control sequence based on geomagnetic gradient information and real-time geomagnetic  $D$  and  $I$  measured by geomagnetic sensors. The simulation results show that our algorithm can successfully reach the location several to tens of nautical miles from the destination under different interferences, such as geomagnetic daily fluctuations, geomagnetic storms, and geomagnetic local anomalies. Likewise, the multi-destination cruise is also simulated, the result of which shows that the AUV can successfully reach the locations near the preset destinations and then return back to the origin. In conclusion, the MPC-based LDUGN approach can achieve the independent underwater navigation and has no accumulation of position error. Combined with other underwater navigation technologies, the accuracy of our method will be further improved.

## ACKNOWLEDGMENT

The authors would like to thank the National Earth System Data Sharing Infrastructure-Geophysical Science Data Center (<http://geospace.geodata.cn/>) and the Chinese Meridian Project (<http://data.meridianproject.ac.cn/>) to provide data support.

## REFERENCES

- [1] A. S. Zaidi and M. R. Suddle, "Global navigation satellite systems: A survey," in *Proc. Int. Conf. Advances Space Technol.*, Islamabad, Pakistan, Sep. 2006, pp. 84–87.
- [2] P. Misra, B. P. Burke, and M. M. Pratt, "GPS performance in navigation," *Proc. IEEE*, vol. 87, no. 1, pp. 65–85, Jan. 1999.
- [3] J. Kinsey, R. Eustice, and L. Whitcomb, "A survey of underwater vehicle navigation: Recent advances and new challenges," in *Proc. IFAC Conf. MCMC*, Lisbon, Portugal, Jan. 2006, pp. 1–12.
- [4] L. Stutters, H. Liu, C. Tiltman, and D. J. Brown, "Navigation technologies for autonomous underwater vehicles," *IEEE Trans. Syst., Man, Cybern. C*, vol. 38, no. 4, pp. 581–589, Jul. 2008.
- [5] A. Stankoff and R. Tait, "Underwater survey using an inertial navigation system," *IEEE Trans. Aerosp. Electron. Syst.*, vol. 3, no. 3, pp. 481–493, May 1977.
- [6] G. T. Donovan, "Position error correction for an autonomous underwater vehicle inertial navigation system (INS) using a particle filter," *IEEE J. Oceanic Eng.*, vol. 37, no. 3, pp. 431–445, Jul. 2012.
- [7] B. Zhao, R. Skjetne, M. Blanke, and F. Dukan, "Particle filter for fault diagnosis and robust navigation of underwater robot," *IEEE Trans. Contr. Syst. Technol.*, vol. 22, no. 6, pp. 2399–2407, Nov. 2014.
- [8] Ø. Hegrehaes and O. Hallingstad, "Model-aided INS with sea current estimation for robust underwater navigation," *IEEE J. Oceanic Eng.*, vol. 36, no. 2, pp. 316–337, Apr. 2011.
- [9] L. Chang, Y. Li, and B. Xue, "Initial alignment for a Doppler velocity log-aided strapdown inertial navigation system with limited information," *IEEE/AMSE Trans. Mechatronics*, vol. 22, no. 1, pp. 329–338, Feb. 2017.
- [10] P. Liu, B. Wang, Z. Deng, and M. Fu, "INS/DVL/PS tightly coupled underwater navigation method with limited DVL measurements," *IEEE Sensors J.*, vol. 18, no. 7, pp. 2994–3002, Apr. 2018.
- [11] M. Morgado, P. Oliveira, C. Silvestre, and J. F. Vasconcelos, "Embedded vehicle dynamics aiding for USBL/INS underwater navigation system," *IEEE Trans. Contr. Syst. Technol.*, vol. 22, no. 1, pp. 322–330, Jan. 2014.
- [12] S. B. Williams, G. Dissanayake, and H. F. Durrant-Whyte, "Towards terrain-aided navigation for underwater robotics," *Adv. Robot.*, vol. 15, no. 5, pp. 533–549, Jan. 2001.
- [13] A. Bar-Gill, P. Ben-Ezra, and I. Y. Bar-Itzhack, "Improvement of terrain-aided navigation via trajectory optimization," *IEEE Trans. Contr. Syst. Technol.*, vol. 2, no. 4, pp. 336–342, Dec. 1994.
- [14] I. Nygren and M. Jansson, "Terrain navigation for underwater vehicles using the correlator method," *IEEE J. Oceanic Eng.*, vol. 29, no. 3, pp. 906–915, Jul. 2004.
- [15] B. Wang, L. Yu, Z. Deng, and M. Fu, "A particle filter-based matching algorithm with gravity sample vector for underwater gravity aided navigation," *IEEE/ASME Trans. Mechatron.*, vol. 21, no. 3, pp. 1399–1408, Jun. 2016.
- [16] Y. Han, B. Wang, Z. Deng, and M. Fu, "A combined matching algorithm for underwater gravity-aided navigation," *IEEE/ASME Trans. Mechatron.*, vol. 23, no. 1, pp. 233–241, Feb. 2018.
- [17] T. Maki, T. Matsuda, T. Sakamaki, T. Ura, and J. Kojima, "Navigation method for underwater vehicles based on mutual acoustical positioning with a single seafloor station," *IEEE J. Oceanic Eng.*, vol. 38, no. 1, pp. 167–177, Jan. 2013.
- [18] B. R. Dzikowicz, B. T. Hefner, and R. A. Leasko, "Underwater acoustic navigation using a beacon with a spiral wave front," *IEEE J. Oceanic Eng.*, vol. 40, no. 1, pp. 177–186, Jan. 2015.
- [19] Z. Song, J. Zhang, W. Zhu, and X. Xi, "The Vector Matching Method in Geomagnetic Aiding Navigation," *Sensors*, vol. 16, no. 7, pp. 1120–1132, Jul. 2016.
- [20] C. Guo, A. Li, C. Hong, and H. Yang, "Algorithm for geomagnetic navigation and its validity evaluation," in *Proc. CSAE*, Shanghai, China, Jul. 2011, pp. 573–577.
- [21] M. Geva-Sagiv, L. Las, Y. Yovel, and N. Ulanovsky, "Spatial cognition in bats and rats: from sensory acquisition to multiscale maps and navigation," *Nat. Rev. Neurosci.*, vol. 16, no. 2, pp. 94–108, Jan. 2015.
- [22] T. E. Dennis, M. J. Rayner, and M. M. Walker, "Evidence that pigeons orient to geomagnetic intensity during homing," *Proc. R. Soc. B, Biol. Sci.*, vol. 274, no. 1614, pp. 1153–1158, May 2007.
- [23] N. F. Putman, K. J. Lohmann, E. M. Putman, T. P. Quinn, A. P. Klimley, and D. L. G. Noakes, "Evidence for geomagnetic imprinting as a homing mechanism in Pacific salmon," *Curr. Biol.*, vol. 23, no. 4, pp. 312–316, Feb. 2013.
- [24] N. F. Putman, E. S. Jenkins, C. G. Michielsens, and D. L. Noakes, "Geomagnetic imprinting predicts spatio-temporal variation in homing migration of pink and sockeye salmon," *J. R. Soc. Interface*, vol. 11, no. 99, pp. 542–551, Oct. 2014.
- [25] P. Luschi, S. Benhamou, C. Girard, S. Ciccione, D. Roos, J. Sudre, and S. Benvenuti, "Marine turtles use geomagnetic cues during open-sea homing," *Curr. Biol.*, vol. 17, no. 2, pp. 126–133, Jan. 2007.
- [26] N. Putman, C. Endres, C. F. Lohmann, and K. J. Lohmann, "Longitude Perception and Bicoordinate Magnetic Maps in Sea Turtles," *Curr. Biol.*, vol. 21, no. 6, pp. 463–466, Mar. 2011.
- [27] J. R. Brothers, K. J. Lohmann, "Evidence that Magnetic Navigation and Geomagnetic Imprinting Shape Spatial Genetic Variation in Sea Turtles," *Curr. Biol.*, vol. 28, no. 8, pp. 1–5, Apr. 2018.
- [28] L. Fiack, N. Cuperlier, and B. Miramond, "Embedded and real-time architecture for bio-inspired vision-based robot navigation," *J. Real-Time Image Proc.*, vol. 10, no. 4, pp. 699–722, Dec. 2015.
- [29] W. Stürzl and H. A. Mallot, "Efficient visual homing based on Fourier transformed panoramic images," *Robot. Auton. Syst.*, vol. 54, no. 4, pp. 300–313, Apr. 2006.
- [30] R. Kapoor, S. Ramasamy, A. Gardi and R. Sabatini, "A bio-inspired acoustic sensor system for UAS navigation and tracking," in *Proc. IEEE 36th Digit. Avion. Syst. Conf.*, Petersburg, USA, Sep. 2017, pp. 1–7.
- [31] Z. Xian, X. Hu, J. Lian, L. Zhang, J. Cao, Y. Wang, and T. Ma, "A Novel Angle Computation and Calibration Algorithm of Bio-Inspired

- Sky-Light Polarization Navigation Sensor,” *Sensors*, vol. 14, no. 9, pp. 17068–17088, Sep. 2014.
- [32] J. Dupeyroux, J. Diperi, M. Boyron, S. Viollet, and J. Serres, “A bio-inspired celestial compass applied to an ant-inspired robot for autonomous navigation,” in *Proc. Eur. Conf. Mobile Robot.*, Paris, France, Sep. 2017, pp. 1–6.
- [33] S. B. Powell, R. Garnett, J. Marshall, C. Rizk, and V. Gruev, “Bioinspired polarization vision enables underwater geolocalization,” *Sci. Adv.*, vol. 4, no. 4, pp. 1–7, Apr. 2018.
- [34] H. Li, M. Liu, and K. Liu, “Bio-inspired geomagnetic navigation method for autonomous underwater vehicle,” *J. Syst. Eng. Electron.*, vol. 28, no. 6, pp. 1203–1209, Dec. 2017.
- [35] Z. Zhao, T. Hu, W. Cui, J. Huangfu, C. Li, and L. Ran, “Long-distance geomagnetic navigation: Imitations of animal migration based on a new assumption,” *IEEE Trans. Geosci. Remote Sens.*, vol. 52, no. 10, pp. 6715–6723, Oct. 2014.
- [36] J. Aubert, J. A. Tarduno, and C. L. Johnson, “Observations and models of the Long-term evolution of Earths magnetic field,” *Space Sci. Rev.*, vol. 155, no. 1, pp. 337–370, Aug. 2010.
- [37] S. Maus and H. Lühr, “Signature of the quiet-time magnetospheric magnetic field and its electromagnetic induction in the rotating Earth,” *Geophys. J. Int.*, vol. 162, no. 3, pp. 755–763, Jul. 2005.
- [38] G. A. Glatzmaier, “Rotation and magnetism of Earths inner core,” *Science*, vol. 274, no. 5294, pp. 1887–1891, Dec. 1996.
- [39] A. Chulliat *et al.* (2014, Dec.) WMM2015\_Report. [Online]. Available: <https://www.ngdc.noaa.gov/geomag/WMM/soft.shtml>
- [40] J. Bloxham, D. Gubbins, A. Jackson, “Geomagnetic secular variation,” *Philos. Trans. R. Soc. Lond.*, vol. 329, no. 1606, pp. 415–502, Nov. 1989.
- [41] J. Li, K. Vahala, and M. G. Suh, “Microresonator Brillouin gyroscope,” *Optica*, vol. 4, no. 3, pp. 346–348, Mar. 2017.
- [42] T. L. Gustavson, P. Bouyer, and M. A. Kasevich, “Precision Rotation Measurements with an Atom Interferometer Gyroscope,” *Phys. Rev. Lett.*, vol. 78, no. 11, pp. 2046–2049, Mar. 1997.
- [43] C. Acar, A. R. Schofield, A. A. Trusov, L. E. Costlow, and A. M. Shkel, “Environmentally Robust MEMS Vibratory Gyroscopes for Automotive Applications,” *IEEE Sensors J.*, vol. 9, no. 12, pp. 1895–1906, Jan. 2009.
- [44] S. J. Qin and T. A. Badgwell, “A survey of industrial model predictive control technology,” *Control Eng. Pract.*, vol. 11, no. 7, pp. 733–764, Jul. 2003.
- [45] C. Wang, X. Liu, X. Yang, F. Hu, A. Jiang, and C. Yang, “Trajectory tracking of an omni-directional wheeled mobile robot using a model predictive control strategy,” *Appl. Sci.*, vol. 8, no. 2, pp. 1–15, Feb. 2018.
- [46] P. Tøndel, T. Johansen, and A. Bemporad, “An algorithm for multiparametric quadratic programming and explicit MPC solutions,” *Automatica*, vol. 39, no. 3, pp. 489–497, Feb. 2003.
- [47] S. Boyd and L. Vandenberghe, “Convex optimization,” *IEEE Trans. Autom. Control*, vol. 51, no. 11, pp. 1859–1864, Nov. 2006.
- [48] R. P. Kane, “Geomagnetic field variations,” *Space Sci. Rev.*, vol. 18, no. 4, pp. 413–540, Jan. 1976.
- [49] W. D. Gonzalez, J. A. Joselyn, Y. Kamide, H.W. Kroehl, G. Rostoker, B.T. Tsurutani, and V.M. Vasylunas, “What is a geomagnetic storm?,” *J. Geophys. Res. Space Phys.*, vol. 99, no. A4, pp. 5771–5792, May 1994.



**Yongding Zhang** received the B.S. degree in computer science and technology from Shaanxi Normal University, Xi’an, China, in 2005 and the M.S. degree in computer application technology from Hefei University of Technology, Hefei, China, in 2013. He is currently pursuing the Ph.D. degree in information and communication engineering, Hohai University, Nanjing, China.

He became a Lecturer in 2015 with the School of Computer and Information Engineering, Chuzhou University, Chuzhou, China. His research interests

include intelligent navigation technology, integrated navigation and intelligent control.



**Xiaofeng Liu** (M’11) received the B.S. degree in electronic engineering and the M.S. degree in computer application from Taiyuan University of Technology, Taiyuan, China, in 1996 and 1999, respectively, and the Ph.D degree in biomedical engineering from XianJiaotong University, Xian, China, in 2006.

In 2006, he joined as an Associate Professor, Shandong University of Science and Technology. From 2008 to 2011, he worked as a Postdoc in the Institute of Artificial Intelligence and Robotics at Xian Jiaotong University. Since 2010, he has been with Hohai University where he is now a Professor and vice Director of the Jiangsu Key Laboratory of Special Robots. His current research interests focus on the study of nature-inspired navigation, human-robot interaction.



**Minzhou Luo** received the M.S. degree in mechatronic engineering from Hefei University of Technology, Hefei, China, in 2002 and the Ph.D. degree in control science and engineering from the University of Science and Technology of China, Hefei, China, in 2005. He is currently with the Jiangsu Key Laboratory of Special Robots (Hohai University). His research interests include bionics, service and industrial robots, and industry 4.0 technology.



**Chenguang Yang** (M’10–SM’16) is a Professor of Robotics. He received the Ph.D. degree in control engineering from the National University of Singapore, Singapore, in 2010 and performed post-doctoral research in human robotics at Imperial College London, London, UK from 2009 to 2010. He has been awarded EU Marie Curie International Incoming Fellowship, UK EPSRC UKRI Innovation Fellowship, and the Best Paper Award of the IEEE Transactions on Robotics as well as over ten conference Best Paper Awards. His research interest lies

in human robot interaction and intelligent system design.